

## UNVEILING MOLECULAR CLOUDS TOWARD BIPOLAR H II REGION G8.14+0.23

L. K. DEWANGAN<sup>1</sup>, H. SANO<sup>2,3</sup>, R. ENOKIYA<sup>3</sup>, K. TACHIARA<sup>3</sup>, Y. FUKUI<sup>2,3</sup>, AND D. K. OJHA<sup>4</sup>

## ABSTRACT

Most recent numerical simulations suggest that bipolar H II regions, powered by O-type stars, can be formed at the interface of two colliding clouds. To observationally understand the birth of O-type stars, we present a detailed multi-wavelength analysis of an area of  $1^\circ \times 1^\circ$  hosting G8.14+0.23 H II region associated with an infrared bipolar nebula (BPN). Based on the radio continuum map, the H II region is excited by at least an O-type star, which is located toward the waist of the BPN. The NANTEN2  $^{13}\text{CO}$  line data reveal the existence of two extended clouds at  $[9, 14.3]$  and  $[15.3, 23.3]$   $\text{km s}^{-1}$  toward the site G8.14+0.23, which are connected in the position-velocity space through a broad-bridge feature at the intermediate velocity range. A “cavity/intensity-depression” feature is evident in the blueshifted cloud, and is spatially matched by the “elongated redshifted cloud”. The spatial and velocity connections of the clouds suggest their interaction in the site G8.14+0.23. The analysis of deep near-infrared photometric data reveals the presence of clusters of infrared-excess sources, illustrating ongoing star formation activities in both the clouds. The O-type star is part of the embedded cluster seen in the waist of the BPN, which is observed toward the spatial matching zone of the cavity and the redshifted cloud. The observational results appear to be in reasonable agreement with the numerical simulations of cloud-cloud collision (CCC), suggesting that the CCC process seems to be responsible for the birth of the O-type star in G8.14+0.23.

*Subject headings:* dust, extinction – H II regions – ISM: clouds – ISM: individual object (G8.14+0.23) – stars: formation – stars: pre-main sequence

## 1. INTRODUCTION

Galactic H II regions excited by O-type stars are considered as complex physical systems, where one can expect the onset of multiple physical processes. Such systems are strongly affected by the intense energetic feedback of O-type stars (i.e., stellar wind, ionized emission, and radiation pressure). However, understanding the exact physical mechanism concerning the birth of O-type stars and young stellar clusters is extremely challenging task in the star formation research, and is still being debated (Zinnecker & Yorke 2007; Tan et al. 2014; Motte et al. 2018). The H II regions are often associated with the extended bubble/ring/bipolar infrared features (e.g., Churchwell et al. 2006, 2007). Furthermore, O-type stars may also trigger new groups of young stellar sources (e.g., Elmegreen & Lada 1977; Bertoldi 1989; Lefloch & Lazareff 1994; Deharveng et al. 2010; Dewangan et al. 2016a).

In the literature, three promising mechanisms are reported for triggering star formation in molecular clouds, which are “globule squeezing”, “collect and collapse”, and “cloud-cloud collision (CCC)” (see Elmegreen 1998, for more details). The first two processes are directly related to the expanding H II regions powered by massive stars, where new generation of star formation is triggered as the gas is swept up (and/or influenced) by the H II re-

gions (e.g., Elmegreen & Lada 1977; Whitworth et al. 1994; Elmegreen 1998; Deharveng et al. 2005; Dale et al. 2007; Bisbas et al. 2015; Walch et al. 2015; Kim et al. 2018; Haid et al. 2019, and references therein).

In the third mechanism, one expects the existence of at least two molecular cloud components in a given star-forming site, which should be connected spatial as well as in velocity space (e.g., Haworth et al. 2015a,b; Torii et al. 2017a, 2018a). In the position-velocity space, the connection of two molecular clouds can be inferred through a feature at the intermediate velocity range, which is indicative of a compressed layer of gas due to the collision of the clouds (e.g., Torii et al. 2017a). The basic results of the existing hydrodynamical simulations of CCC are that the CCC process has ability to form massive clumps and cores at the junction of molecular clouds or the shock-compressed interface layer (e.g., Habe & Ohta 1992; Anathpindika 2010; Inoue & Fukui 2013; Takahira et al. 2014, 2018; Haworth et al. 2015a,b; Wu et al. 2015, 2017a,b; Torii et al. 2017a; Balfour et al. 2017; Bisbas et al. 2017; Whitworth et al. 2018, and references therein), where the initial conditions are suitable for the formation of massive stars and clusters of young stellar objects (YSOs). In particular, Whitworth et al. (2018) discussed the formation of bipolar H II regions through the CCC process. However, to our knowledge, observational investigations of such sites are rare in the literature. In this connection, the present paper is focused to observationally study a promising bipolar H II region G8.14+0.23 to explore the theoretical scenarios concerning the formation of bipolar H II regions hosting massive stars and embedded clusters.

The G8.14+0.23/IRAS 17599–2148 is classified as a bipolar blister type H II region powered by an O6 spectral class source (e.g., Kim & Koo 2001, 2003). The

lokeshd@prl.res.in

<sup>1</sup> Physical Research Laboratory, Navrangpura, Ahmedabad - 380 009, India.<sup>2</sup> Institute for Advanced Research, Nagoya University, Furo-cho, Chikusa-ku, Nagoya 464-8601, Japan.<sup>3</sup> Department of Physics, Nagoya University, Furo-cho, Chikusa-ku, Nagoya 464-8601, Japan.<sup>4</sup> Department of Astronomy and Astrophysics, Tata Institute of Fundamental Research, Homi Bhabha Road, Mumbai 400 005, India.

G8.14+0.23 H II region is associated with a bipolar nebula (BPN) containing two mid-infrared (MIR) bubbles (CN107 and CN109; Churchwell et al. 2007). Using the integrated NANTEN  $^{12}\text{CO}$  intensity map (beam size  $\sim 2''.6$ ), the site G8.14+0.23 is seen in the direction of a molecular cloud M008.2+0.2 (having a radial velocity range of  $\sim 12\text{--}25\text{ km s}^{-1}$ ; Takeuchi et al. 2010). The star-forming site also hosts a Class II 6.7 GHz methanol maser (peak velocity  $\sim 19.83\text{ km s}^{-1}$ ; Szymczak et al. 2012) in the direction of the waist of the BPN. In general, the 6.7 GHz methanol maser is considered as a good indicator of massive young stellar objects (MYSOs) (e.g. Walsh et al. 1998; Urquhart et al. 2013). Using a multi-wavelength approach, Dewangan et al. (2012) (hereafter Paper I) and Dewangan et al. (2016b) (hereafter Paper II) reported star formation activities toward the edges of the BPN as well as its waist, and pointed out an interaction of the H II region with its surroundings. On a large-scale study of G8.14+0.23 in Paper II, the site has been found to be embedded in an elongated filamentary structure (EFS) traced in the *Herschel* maps. Furthermore, *Herschel* clumps and clusters of YSOs have also been observed toward the EFS. Together, the earlier studies indicate the presence of young stellar clusters and massive stars in the site G8.14+0.23. However, a detailed study of the distribution of molecular gas associated with the site G8.14+0.23 is yet to be performed. Figure 1a shows the *Herschel* image at  $250\text{ }\mu\text{m}$  (size  $\sim 1^\circ \times 1^\circ$ ) overlaid with the NRAO VLA Sky Survey (NVSS;  $\lambda = 21\text{ cm}$ ; resolution =  $45''$ ; Condon et al. 1998) continuum emission contours (in red). The APEX Telescope Large Area Survey of the Galaxy (ATLASGAL;  $\lambda = 870\text{ }\mu\text{m}$ ; resolution =  $19''.2$ ; ATLASGAL; Schuller et al. 2009) dust clumps (from Urquhart et al. 2018) are also marked in the *Herschel*  $250\text{ }\mu\text{m}$  image. In Figure 1a, sixteen clumps highlighted with square symbols (in blue) are traced in a velocity range of  $[15, 21]\text{ km s}^{-1}$ , and at a distance of  $3.0\text{ kpc}$  (e.g., Urquhart et al. 2018). Previously, Kim & Koo (2001) reported a distance of  $4.2\text{ kpc}$  to G8.14+0.23. Urquhart et al. (2018) made an attempt to solve the distance ambiguity of the observed ATLASGAL clumps. Hence, in this paper, we have considered the distance of  $3.0\text{ kpc}$  for the site G8.14+0.23.

In order to carefully examine the large-scale molecular environment and star formation activities, we have employed new NANTEN2  $^{13}\text{CO}$  ( $J=1-0$ ) line data and deep UKIDSS near-infrared (NIR) photometric data. Such analysis provides a promising step for observationally understanding the exact birth process of massive star(s), BPN, and clusters of YSOs in the site G8.14+0.23.

This paper is organized as follows. In Section 2, we introduce the observational data sets adopted in this paper. Then, Section 3 deals with the new results obtained through a multi-wavelength approach. Star formation mechanism operational in the site G8.14+0.23 is discussed in Section 4. Finally, we conclude in Section 5.

## 2. DATA SETS AND ANALYSIS

The present paper deals with an area of  $\sim 1^\circ \times 1^\circ$  ( $\sim 52.3\text{ pc} \times 52.3\text{ pc}$ ; centered at  $l = 8^\circ.14$ ;  $b = 0^\circ.239$ ) containing the site G8.14+0.23.

### 2.1. New Observations

#### 2.1.1. $^{13}\text{CO}$ ( $J=1-0$ ) Line Data

Observations of  $^{13}\text{CO}$  ( $J=1-0$ ) emission line at  $110.201353\text{ GHz}$  were carried out in January 2013 using the NANTEN2 4m millimeter/sub-millimeter radio telescope of Nagoya University installed at Pampa La Bola (4865m above sea level), in Chile. We mapped an area of  $1^\circ \times 1^\circ$  centered at G8.14+0.23, using the on-the-fly mapping technique with a Nyquist sampling. The front-end was a 4 K cooled Nb superconductor-insulator-superconductor mixer receiver. The back-end was a digital Fourier-transform spectrometer with 16384 channels (1 GHz bandwidth), corresponding to a velocity coverage of  $\sim 2700\text{ km s}^{-1}$  and a velocity resolution of  $\sim 0.17\text{ km s}^{-1}$ . A typical system temperature including the atmosphere is  $\sim 130\text{ K}$  in the double side band. The absolute intensity was calibrated by observing Rho Oph and M17SW [ $(\alpha_{2000}, \delta_{2000}) = (18^h 20^m 24.4^s, -16^\circ 13' 17''.6)$ ]. We also checked the pointing accuracy every two hours to satisfy a pointing offset within  $30''$  by observing Jupiter and IRC+10216. After convolution with a two dimensional Gaussian function having a full width at half maximum (FWHM) of  $90''$ , we obtained the final beam size of  $\sim 200''$  (or  $\sim 2.9\text{ pc}$  at a distance of  $3.0\text{ kpc}$ ). The noise fluctuation is  $\sim 0.5\text{ K}$  at a velocity resolution of  $\sim 0.5\text{ km s}^{-1}$ .

#### 2.2. Archival data sets

In this paper, we also adopted multi-frequency data sets retrieved from different existing Galactic plane surveys. The ionized emission and the dust clumps at  $870\text{ }\mu\text{m}$  are studied using the NVSS  $1.4\text{ GHz}$  map and the ATLASGAL  $870\text{ }\mu\text{m}$  data, respectively. The *Herschel* Infrared Galactic Plane Survey (Hi-GAL;  $\lambda = 70, 160, 250, 350, 500\text{ }\mu\text{m}$ ; resolutions =  $5'', 8'', 12'', 18'', 25'', 37''$ ; Molinari et al. 2010) data are utilized to study the far-infrared (FIR) and sub-millimeter (mm) emission. To explore the mid-infrared (MIR)  $8.0\text{ }\mu\text{m}$  emission, the Galactic Legacy Infrared Mid-Plane Survey Extraordinaire (GLIMPSE;  $\lambda = 3.6, 4.5, 5.8, 8.0\text{ }\mu\text{m}$ ; resolution  $\sim 2''$ ; Benjamin et al. 2003) data are used. To examine the sources with infrared-excess emission, the UKIRT NIR Galactic Plane Survey (GPS;  $\lambda = 1.25, 1.65, 2.2\text{ }\mu\text{m}$ ; resolution  $\sim 0''.8$ ; Lawrence et al. 2007) and the Two Micron All Sky Survey (2MASS;  $\lambda = 1.25, 1.65, 2.2\text{ }\mu\text{m}$ ; resolution =  $2''.5$ ; Skrutskie et al. 2006)) data are employed. More information of these selected data sets can be found in Dewangan (2017) and Dewangan et al. (2017a).

## 3. RESULTS

### 3.1. Large-scale spatial view of G8.14+0.23

The observed sub-mm continuum and molecular line data are utilized to explore a wide-field area of the site G8.14+0.23. In Figure 1a, the sub-mm image at  $250\text{ }\mu\text{m}$ , the NVSS radio continuum emission, and the ATLASGAL dust continuum clumps at  $870\text{ }\mu\text{m}$  are presented (see also Section 1). The *Herschel* image at  $350\text{ }\mu\text{m}$  is also presented in Figure 1b. A qualitative information of the distribution of the cold dust emission can be gathered from the ATLASGAL and *Herschel* sub-mm images (see Figure 1 and also Section 3.2 for a quantitative estimate). The previously known BPN is also seen in the *Herschel* images, and is highlighted by a white dashed box in Figure 1b. In Figure 1b, we have also marked

an area by a solid box (in white), which was studied in Paper II. The position of the 6.7 GHz methanol maser is also shown in Figures 1a and 1b. As mentioned before, the 6.7 GHz methanol maser is a reliable agent for tracing MYSOs (e.g., Walsh et al. 1998; Urquhart et al. 2013). The peak position of the radio continuum emission and the 6.7 GHz maser are observed toward the waist of the BPN (see also Paper I). High resolution GMRT radio continuum maps of the G8.14+0.23 H II region were presented in Paper II. Furthermore, in Paper II, an infrared counterpart of the 6.7 GHz maser was identified with the absence of radio continuum emission, and its inner environment ( $< 5000$  AU) was also examined using the high resolution NIR images. Different evolutionary phases of massive stars have been reported toward the waist of the BPN (see Paper II for more details).

Using the NANTEN2  $^{13}\text{CO}$  ( $J=1-0$ ) line data, we have produced the  $^{13}\text{CO}$  intensity (moment-0) map, which is displayed in Figure 2a. The molecular emission is integrated over a velocity range of  $[8, 25]$   $\text{km s}^{-1}$ . The moment-0 map is also overlaid with the  $^{13}\text{CO}$  emission contours, revealing an extended molecular cloud in the direction of the site G8.14+0.23 (see Figure 2a). Using the *Spitzer* 8  $\mu\text{m}$  image, a zoomed-in view of the BPN is presented in Figure 2b. The NVSS 1.4 GHz emission contour (in white) is also shown in the figure, indicating the location of the G8.14+0.23 H II region. In Paper I, the dynamical age of the H II region powered by an O6.5-O6 star was reported to be  $\sim 1.6$  Myr. All the calculations were performed using a distance of 4.2 kpc (see Paper I).

Following the same methods adopted in Paper I and considering the new distance to G8.14+0.23 (i.e.,  $d = 3.0$  kpc), we have also estimated the number of Lyman continuum photons ( $N_{uv}$ ) (see equation 1 in Paper II and also Matsakis et al. 1976) and the dynamical age of the H II region (e.g., Dyson & Williams 1980). Using the NVSS 1.4 GHz data, the analysis is carried out for an electron temperature of  $10^4$  K and a distance of 3.0 kpc. The analysis yields  $N_{uv}$  (or  $\log N_{uv}$ ) to be  $\sim 4.28 \times 10^{48}$   $\text{s}^{-1}$  (48.63) for the G8.14+0.23 H II region, which refers to a single ionizing star of spectral type O8-O7.5V (Panagia 1973). It is indeed obvious that at least an O-type star is present toward the waist of the BPN.

The equation of the dynamical age of the H II region (Dyson & Williams 1980) is given by

$$t_{dyn} = \left( \frac{4R_s}{7c_s} \right) \left[ \left( \frac{R_{HII}}{R_s} \right)^{7/4} - 1 \right] \quad (1)$$

where  $c_s$  is the isothermal sound velocity in the ionized gas ( $c_s = 11$   $\text{km s}^{-1}$ ; Bisbas et al. (2009)),  $R_{HII}$  is the radius of the H II region ( $R_{HII} \sim 2.3$  pc), and  $R_s$  is the radius of the Strömgren sphere ( $= (3 N_{uv}/4\pi n_0^2 \alpha_B)^{1/3}$ , where the radiative recombination coefficient  $\alpha_B = 2.6 \times 10^{-13}$  ( $10^4$  K/T) $^{0.7}$   $\text{cm}^3 \text{s}^{-1}$  (Kwan 1997),  $N_{uv}$  ( $\sim 4.28 \times 10^{48}$   $\text{s}^{-1}$ ) is defined earlier, and “ $n_0$ ” is the initial particle number density of the ambient neutral gas). Adopting the values of  $N_{uv}$ ,  $R_{HII}$ , and  $c_s$ , we have determined the dynamical age of the G8.14+0.23 H II region to be  $\sim 0.3(1.1)$  Myr for  $n_0$  of  $10^3(10^4)$   $\text{cm}^{-3}$ .

### 3.2. *Herschel* temperature and column density maps

Figures 3a and 3b present the *Herschel* temperature and column density maps of a large-scale area containing the G8.14+0.23 H II region. In Paper II, we described the procedures for producing these maps (see also Mallick et al. 2015, for more details). The contours of the integrated intensity map of  $^{13}\text{CO}$  ( $J=1-0$ ) at  $[8, 25]$   $\text{km s}^{-1}$  are also overlaid on both the *Herschel* maps (see also Figure 2a). The EFS and the BPN are seen within the  $^{13}\text{CO}$  emission contour with a level of  $16.66$  K  $\text{km s}^{-1}$  (see Figure 3b). To highlight the location of the G8.14+0.23 H II region, the NVSS 1.4 GHz continuum emission contour is marked in the maps. In Figure 3a, the temperature contour at 23 K is also superimposed on the *Herschel* temperature map, tracing an extended temperature feature. The observed temperature feature seems to be more extended compared to the radio continuum emission traced in the NVSS map, depicting the signatures of the feedback from the clusters of YSOs as well as the impact of the ionizing photons of the O-type star (see Paper II and also Section 3.4 in this paper). In Figure 3b, a comparison of the distribution of molecular gas against the dust column density distribution can be examined, revealing locations of high dust column density ( $N(\text{H}_2) \sim 10\text{--}35 \times 10^{21}$   $\text{cm}^{-2}$  or  $A_V \sim 10.5\text{--}37.5$  mag) within the cloud. Using the value of  $N(\text{H}_2)$ , a conversion expression (i.e.,  $A_V = 1.07 \times 10^{-21} N(\text{H}_2)$ ; Bohlin et al. 1978) is utilized to determine the extinction information along the line of sight.

### 3.3. *Molecular cloud components*

As mentioned earlier, a detailed study of molecular gas in a wide-scale environment of G8.14+0.23 is missing in the literature. To examine the distribution of molecular gas in our selected target field, Figures 4a and 4b display the  $^{13}\text{CO}$  moment-0 and moment-1 maps overlaid with the contour of the integrated intensity map of  $^{13}\text{CO}$  at  $[8, 25]$   $\text{km s}^{-1}$ , respectively. In Figure 4, one can compare the moment-0 map against the moment-1 map. The  $^{13}\text{CO}$  moment-0 map is the same as shown in Figure 2a. In order to produce the moment-1 map, the  $^{13}\text{CO}$  emission is integrated over the velocity range of  $[8, 25]$   $\text{km s}^{-1}$ , and is clipped at the  $4.8\sigma$  rms level of  $\sim 0.44$  K per channel. Figure 4b enables us to examine the intensity-weighted mean velocity of the emitting gas, indicating the presence of two molecular cloud components in the direction of the site G8.14+0.23.

In Figure 5, we display the integrated  $^{13}\text{CO}$  velocity channel maps from 9 to 25  $\text{km s}^{-1}$ . In Figure 5, each panel is generated by integrating the emission over 1  $\text{km s}^{-1}$  velocity intervals, and the observed temperature feature (see dotted red curve) and the location of the G8.14+0.23 H II region (see solid blue contour) are also marked. We find the existence of two molecular cloud components (around 11.5 and 18.5  $\text{km s}^{-1}$ ) in the direction of the site G8.14+0.23.

To further explore the different molecular components, we display the latitude-velocity and longitude-velocity maps of  $^{13}\text{CO}$  in Figures 6a and 6b, respectively. Note that the position-velocity maps of  $^{13}\text{CO}$  are extracted for an area, which is marked in Figure 4a (see a solid box in Figure 4a). In the direction of this selected area, the majority of the molecular emission is distributed. Both these position-velocity maps show two velocity compo-

nents around 11.5 and 18.5 km s<sup>-1</sup> (see dotted lines in Figures 6a and 6b). The velocity gradients are evident in Figure 6a. In the position-velocity space, we find a broad-bridge feature at the intermediate velocity range between two velocity components around 11.5 and 18.5 km s<sup>-1</sup> (see an arrow in Figure 6b). In Figure 6c, we have presented the spatial distribution of molecular gas in two clouds at [9, 14.3] and [15.3, 23.3] km s<sup>-1</sup>. Very weak <sup>13</sup>CO emission is observed toward the central part of the cloud component at [9, 14.3] km s<sup>-1</sup> (see Figure 6c). It implies the presence of an intensity-depression in the molecular cloud at [9, 14.3] km s<sup>-1</sup>, which is referred to as “cavity” feature. The BPN and the EFS are associated with the cloud component at [15.3, 23.3] km s<sup>-1</sup>. We find a spatial match between the cloud at [15.3, 23.3] km s<sup>-1</sup> and the “cavity” present in the cloud at [9, 14.3] km s<sup>-1</sup> (see Figure 6c). In addition, some overlapping zones of these two different clouds are also indicated in Figure 6c (see arrows in Figure 6c).

To further explore the broad-bridge feature, we have generated the observed <sup>13</sup>CO profile toward an area marked in Figure 4b (see a solid box in Figure 4b). The selected area is seen in the direction of both the clouds. The observed <sup>13</sup>CO profile is shown in Figure 6d, and is computed by averaging the selected area. The spectrum has almost flattened profile between two velocity peaks around 11.5 and 18.5 km s<sup>-1</sup>, further indicating the presence of the bridge feature. In this context, new molecular line data with better sensitivity and/or resolution will be further helpful.

A detailed discussions on all these results are presented in Section 4.

### 3.4. Young stellar populations

In Paper I and Paper II, the studies concerning the selection of YSOs were performed for an area highlighted by a solid box in Figure 1b. In this paper, we have identified YSOs for a much wider area around the site G8.14+0.23 (see Figure 1a). To examine the sources with infrared-excess emission, we have used the NIR color-magnitude plot (H–K/K), as adopted in Paper II. The reliable NIR HK photometric magnitudes of point-like sources in our selected target region were obtained from the UKIRT Infrared Deep Sky Survey (UKIDSS) 6<sup>th</sup> archival data release (UKIDSSDR6plus) of the Galactic Plane Survey (GPS) and 2MASS catalog (see Paper II for more details and also Dewangan et al. 2015b). In Paper II, a color condition (i.e., H–K > 2.2 mag (or A<sub>V</sub> = 35.5 mag); Indebetouw et al. 2005) was selected to identify a population of sources with infrared-excess emission. To obtain this condition, the color-magnitude analysis of sources located in a nearby control field was carried out (see Paper II). In our selected target area, we find 2150 deeply embedded sources with H–K > 2.2 mag, which are overlaid on the *Herschel* 250 μm and molecular maps (see Figure 7a). The <sup>13</sup>CO emission contours at [8, 25] km s<sup>-1</sup> are also superimposed on the *Herschel* image. In Figure 7b, we have also shown surface density contours of these embedded sources, which are overlaid on the molecular maps at [9, 14.3] and [15.3, 23.3] km s<sup>-1</sup>. The nearest-neighbour (NN) technique is adopted to derive the surface density contours of selected YSOs (see Casertano & Hut 1985; Gutermuth et al. 2009; Bressert

et al. 2010; Dewangan et al. 2015a,b; Dewangan 2017; Dewangan et al. 2017a, for more details). Following the work of Dewangan et al. (2015a), we have generated the surface density map of all the selected embedded sources using a 10'' grid and 6 NN at a distance of 3.0 kpc. To infer embedded clusters in star-forming regions, Lada & Lada (2003) considered the minimum surface density of 3 YSO pc<sup>-2</sup>. Hence, in Figure 7b, the surface density contours of YSOs are displayed with the levels of 3, 5, and 10 YSOs pc<sup>-2</sup>, enabling us to depict the groups of YSOs (e.g., Lada & Lada 2003; Bressert et al. 2010). The groups of YSOs are seen toward both the cloud components at [9, 14.3] and [15.3, 23.3] km s<sup>-1</sup>, revealing a spatial correlation between embedded clusters and molecular gas. This analysis helps us to depict the star-forming zones in the extended molecular clouds, suggesting the ongoing star formation activities in both the clouds.

Figure 8a shows a zoomed-in view of an area containing the EFS and the BPN. In Figure 8a, the surface density contours are superimposed on the *Spitzer* 8.0 μm image (see also Figure 7b). With the help of the surface density analysis, the clusters of YSOs are spatially seen toward the EFS (see also Paper II). The signatures of star formation are also observed toward the edges and the waist of the BPN (see also Paper I and Paper II). In Figure 8b, we present the distribution of the clouds at [9, 14.3] and [15.3, 23.3] km s<sup>-1</sup> in the direction of the same area as shown in Figure 8a. The background contour map represents the cloud at [9, 14.3] km s<sup>-1</sup>, while the red contours refer to the cloud at [15.3, 23.3] km s<sup>-1</sup>. The NVSS radio continuum contour and the temperature contour at 23 K are also shown in both Figures 8a and 8b. It seems that the star formation activities and the feedback of the massive star may have heated the surroundings, which could be responsible for the extended temperature feature (see also Section 3.2). Altogether from Figures 8a and 8b, the clusters of YSOs are observed toward the spatial matching zone of the elongated redshifted cloud at [15.3, 23.3] km s<sup>-1</sup> and the “cavity” feature depicted in the cloud at [9, 14.3] km s<sup>-1</sup>, where the exciting star of the G8.14+0.23 H II region and the 6.7 GHz maser are investigated.

## 4. DISCUSSION

In Paper I, the bipolar morphology, as the most prominent structure in the infrared images, was investigated in the G8.14+0.23 H II region, which was also found to be part of the EFS (see Paper II). In Paper I and Paper II, the star formation in the periphery of the BPN was explained by the ionizing feedback of the massive star. In Section 3.1, we have reported the indicative value of the dynamical age of the G8.14+0.23 H II region to be ~0.3(1.1) Myr for n<sub>0</sub> of 10<sup>3</sup>(10<sup>4</sup>) cm<sup>-3</sup>. Earlier, Evans et al. (2009) reported a mean age of YSOs to be ~0.44–2 Myr. Hence, the formation of the clusters of YSOs seen toward the edges of the BPN could be influenced by the positive feedback of the O-type star (see also Paper I and Paper II). However, in Paper II, it was also suggested that the observed clusters of YSOs in the direction of the EFS were not triggered by the impact of the O-type star, and might have spontaneously formed. This argument was suggested based on the estimation of the pressure of the H II region, which was found to be very

low (see Paper II for more details). It implies that the birth of the O-type star is not well understood, which is the main goal of this observational work. In this context, we have performed a careful observational study of the molecular gas distribution for  $\sim 1^\circ \times 1^\circ$  area around the site G8.14+0.23, which has not been conducted before for the selected target (see Section 3.3).

Habe & Ohta (1992) and Torii et al. (2015) performed numerical simulations of head-on collisions of two dissimilar clouds to study the CCC process. In their simulations, gravitationally unstable cores/clumps at the interface of the clouds were produced by the effect of their compression. A cavity was also created in the large cloud, and massive stars were formed at the interface of clouds. After the birth of massive stars, their strong UV radiation produced an H II region. Subsequently, the cavity in the large cloud was filled with the ionized emission powered by massive stars (Torii et al. 2015). Inoue & Fukui (2013) carried out magnetohydrodynamical numerical simulations of the CCC process, and studied the physical conditions of the interface layer. They found that the collision process significantly enhances the sound speed and the mass accretion rate. It was also reported that in the direction of the interface layer, the O-type star can be formed within  $\sim 0.1$  Myr at a mass accretion rate of  $10^{-4} M_\odot \text{ yr}^{-1}$  (see also Fukui et al. 2018a). In a very recent simulations, Whitworth et al. (2018) found the formation of a bipolar H II region via the collisions of two clouds. In the simulations, a star cluster containing ionizing stars can be formed near the center of the shock-compressed layer. Then, the H II region powered by the ionizing stars can expand rapidly in the directions perpendicular to the layer, leading to the formation of a bipolar H II region. Hence, it is expected that massive stars and young stellar clusters can be produced at the waist of the bipolar H II region or the shock-compressed layer (see also Inoue & Fukui 2013), where one can obtain high column density materials ( $\geq 10^{22} \text{ cm}^{-2}$ ).

Several observational works on the CCC process are also available in the literature (e.g., Loren 1976; Miyawaki et al. 1986, 2009; Hasegawa et al. 1994; Sato et al. 2000; Okumura et al. 2001; Furukawa et al. 2009; Ohama et al. 2010, 2017, 2018a,b; Shimoikura & Dobashi 2011; Torii et al. 2011, 2015, 2017a,b, 2018a,b; Nakamura et al. 2012, 2014; Shimoikura et al. 2013; Dobashi et al. 2014; Fukui et al. 2014, 2015, 2016, 2017, 2018a,b,c,d; Haworth et al. 2015a,b; Tsuboi et al. 2015; Baug et al. 2016; Dewangan 2017; Dewangan & Ojha 2017; Dewangan et al. 2017b, 2018a,b; Fujita et al. 2017, 2018; Gong et al. 2017; Liu et al. 2017; Nishimura et al. 2017, 2018; Saigo et al. 2017; Sano et al. 2017, 2018; Tsutsumi et al. 2017; Enokiya et al. 2018; Hayashi et al. 2018; Kohno et al. 2018a,b; Li et al. 2018; Tachihara et al. 2018; Takahira et al. 2018; Tsuge et al. 2018), where one can find observational signposts of the CCC process. As highlighted previously, one expects a spatial and velocity connection of two clouds in the CCC process (e.g. Torii et al. 2017a). In the position-velocity map, the link of blueshifted and redshifted clouds via a lower intensity intermediate velocity emission (i.e. bridge feature) illustrates the velocity connection (e.g., Haworth et al. 2015a,b). As mentioned earlier, the bridge feature might trace a compressed layer of gas due to the collision of the clouds (e.g., Torii et

al. 2017a). One can also find the presence of a complementary spatial distribution of clouds in the CCC site, which is related to the spatial fit of “Keyhole/intensity-depression” and “Key/intensity-enhancement” features (e.g., Torii et al. 2017a; Fukui et al. 2018a). In the CCC process, after the collision of two clouds, massive stars and clusters of YSOs can be seen in the shocked-compressed layer of the clouds, and a cavity filled with the ionized emission excited by massive stars can be found in one of the clouds.

Keeping in mind these observational features of the CCC, at least two molecular cloud components (around 11.5 and 18.5  $\text{km s}^{-1}$ ) are investigated in the direction of the site G8.14+0.23 (see Figures 4b, 5, 6a, and 6b). Various observed components related to the site G8.14+0.23 are summarized in Figure 9a. This figure illustrates a complementary spatial distribution of clouds (i.e., spatial fit between the cavity in the blueshifted cloud and the elongated redshifted cloud; see a solid box in Figure 9a). The cavity or intensity-depression in the blueshifted cloud is highlighted by a broken hexagonal (see Figure 9b), while the redshifted cloud is shown in Figure 9c. In the position-velocity space, the signature of the bridge feature between the two clouds is also found (see Section 3.3 and also Figure 6). An almost V-shaped velocity structure is also seen in the position-velocity map (see Figure 6a), which can be originated in the position-velocity space due to the combination of the intensity-depression/cavity and the bridge feature (e.g., Anathpindika 2010; Fukui et al. 2018a,c). High-resolution and better sensitivity molecular line data will be needed to gain more information regarding the V-shaped velocity structure. Altogether these observational facts are consistent with the signatures of the CCC scenario. Therefore, it appears that the observed molecular morphology hints the post-collision condition in the site G8.14+0.23 (see Figure 9a). The “elongated redshifted cloud” is analogous to the shock-compressed layer as seen in the simulations of the CCC process. The shock-compressed layer is expected at the location of impact in the post-collision condition, whereas the “cavity” in the blueshifted cloud denotes the collision site (e.g., Torii et al. 2017a). Hence, before the collision process, no cavity was predicted in the blueshifted cloud. In the direction of the BPN, the column densities are observed in the range of  $\sim 1.8\text{--}3.5 \times 10^{22} \text{ cm}^{-2}$  ( $A_V \sim 19\text{--}37$  mag). Furthermore, the present data do not allow to obtain the exact information of the viewing angle of the collision to the line of sight. With the knowledge of the distribution of the cavity and the elongated redshifted cloud, the collision of two clouds might had taken place in the Galactic northern-western direction (see a broken line in Figure 9a), where the BPN is seen. Hence, the broken line may indicate the direction of the relative motion of the two clouds (see Figure 9a).

Note that the signposts of massive stars (i.e., H II region and 6.7 GHz methanol maser), the embedded clusters, the BPN, and the extended temperature feature are observed toward the spatial matching zone of the cavity and the redshifted cloud/shock-compressed layer (see Figure 8 and also a solid box in Figure 9a). In order to infer the impact of the CCC, the information of the collision time-scale is essential. Following the equation given in McKee & Ostriker (2007), one can estimate the

collision time-scale using the relative velocity of the two clouds, collision length-scale, and ratio of number densities of post-collision and pre-collision regions (see also equation 2 in Henshaw et al. 2013). The time-scale of the accumulation of material at the collision points or the collision time-scale (McKee & Ostriker 2007; Henshaw et al. 2013) can be computed using the expression below:

$$t_{\text{accum}} = 2.0 \left( \frac{l_{\text{ccc}}}{0.5 \text{ pc}} \right) \left( \frac{v_{\text{rel}}}{5 \text{ km s}^{-1}} \right)^{-1} \left( \frac{n_{\text{pstccc}}/n_{\text{preccc}}}{10} \right) \text{ Myr} \quad (2)$$

where,  $l_{\text{ccc}}$  is the collision length-scale,  $v_{\text{rel}}$  is the relative velocity of clouds,  $n_{\text{preccc}}$  is the mean density of pre-collision region, and  $n_{\text{pstccc}}$  is the mean density of post-collision region. In the calculation, we have assumed a viewing angle ( $= 45^\circ$ ) of the collision to the line of sight. In Section 3.1, we have used the size of the H II region (i.e.  $2 \times R_{\text{HII}}$ ) to be  $\sim 4.5$  pc, where the ionized emission is spatially distributed (see Figure 8a). Hence, we have used the size of the H II region to estimate the collision length-scale ( $l_{\text{ccc}}$ ), which is adopted to be  $\sim 6.4$  pc ( $= 4.5 \text{ pc}/\sin(45^\circ)$ ). In the direction of the site G8.14+0.23, the velocity separation of the two clouds is  $\sim 7 \text{ km s}^{-1}$ . It gives the observed relative velocity ( $v_{\text{rel}}$ ) to be  $\sim 10 \text{ km s}^{-1}$  ( $= 7 \text{ km s}^{-1}/\cos(45^\circ)$ ). Note that in this paper, the existing observational data sets do not allow us to determine the exact ratio of the mean densities of the pre- and post-collision regions. In the collision process, one can expect the increase of density in the post-collision region against the pre-collision site. Hence, the density ratio is expected to be larger than unity (i.e.  $n_{\text{pstccc}}/n_{\text{preccc}} > 1$ ). If we use a range of the ratios of densities (i.e., 1–10) in equation 2 then the collision timescale range is estimated to be  $\sim 1.28$ – $12.8$  Myr.

In Section 3.1, the dynamical age of the G8.14+0.23 H II region is computed to be  $\sim 0.3(1.1)$  Myr for the ambient density of  $10^3(10^4) \text{ cm}^{-3}$ . In this analysis, the spherical morphology of the H II region was assumed, which evolved into the homogeneous medium (see Dyson & Williams 1980, for more details). Both these assumptions are unlikely for the G8.14+0.23 H II region. Therefore, the dynamical age of the H II region as well as the collision timescale can be considered as indicative values. Despite the uncertain nature of these calculations, the ratio of the dynamical age of the H II region and the timescale for mass build up during the collision process appears to be less than unity (i.e.,  $t_{\text{dyn}}/t_{\text{accum}} < 1$ ), which indicates that the proposed hypothesis is plausible. Additionally, in the site, the early phase of massive star formation ( $< 0.1$  Myr) has also been reported through the detection of the 6.7 GHz methanol maser (see Paper II). In the numerical simulations, the O-type star is formed within a few times of  $10^5$  yr (Inoue & Fukui 2013). It appears that the CCC process began before the formation of massive stars in our selected site. Hence, the birth of the O-type star located in the waist of the BPN seems to be triggered by the CCC process (see also the simulation of Whitworth et al. 2018). Note that star formation activities toward the edges of the BPN could also be triggered by the O-type star, which we cannot entirely rule out.

Our case study of the bipolar H II region G8.14+0.23

encourages us to examine the CCC process in other known sample of Galactic bipolar H II regions (e.g., Churchwell et al. 2006, 2007), which will further allow us to observationally assess the existing theoretical simulations concerning the triggered O-type star formation on the waist of the bipolar H II regions.

## 5. SUMMARY AND CONCLUSIONS

To understand the formation of massive stars and young stellar clusters, a large-scale area of the site G8.14+0.23 (size  $\sim 1^\circ \times 1^\circ$ ) is investigated using a multi-wavelength approach. The major outcomes of this paper are as follows:

- The G8.14+0.23 H II region, having a dynamical age of  $\sim 0.3(1.1)$  Myr for  $n_0$  of  $10^3(10^4) \text{ cm}^{-3}$ , is powered by at least an O-type star, which is observed toward the waist of the BPN.
- The NANTEN2  $^{13}\text{CO}$  line data trace molecular gas associated with the site G8.14+0.23 in a velocity range of  $[8, 25] \text{ km s}^{-1}$ . Furthermore, two extended molecular cloud components at  $[9, 14.3]$  and  $[15.3, 23.3] \text{ km s}^{-1}$  are unveiled toward the selected site. The data have also shown their physical connection in both space and velocity.
- A spatial complementary distribution concerning the collisions of two clouds is found in the selected site. A “cavity/intensity-depression” feature is evident in the blueshifted cloud (i.e.,  $[9, 14.3] \text{ km s}^{-1}$ ), and is spatially matched by the elongated redshifted cloud (i.e.,  $[15.3, 23.3] \text{ km s}^{-1}$ ). A broad-bridge feature is also identified in the position-velocity space.
- With the help of deep NIR photometric data of point-like sources, a total of 2150 embedded sources with  $H-K > 2.2$  mag are identified in the selected target field. Groups of the embedded infrared-excess sources are observed in both the clouds (including the EFS and the BPN).
- The *Herschel* temperature map shows an extended temperature structure ( $T_d = 23$ – $36$  K) in the direction of the G8.14+0.23 H II region.
- Signposts of massive star formation (i.e., 6.7 GHz methanol maser and H II region), the BPN, the embedded clusters, and the extended temperature structure are found toward the spatial matching zone of the cavity and the redshifted cloud. In the direction of this matching zone, the column densities are found to be  $\sim 1.8$ – $3.5 \times 10^{22} \text{ cm}^{-2}$  (or  $A_V \sim 19$ – $37$  mag).
- The outcomes of the present work suggest the interaction of molecular clouds in the site G8.14+0.23.

Considering our new observational findings in this paper, we suggest that the CCC scenario can explain the star formation history in the site G8.14+0.23. Our observed results are in qualitative agreement with the proposed numerical simulations of the CCC. In this connection, new molecular line data with better sensitivity and high-resolution will be further useful.

We thank the anonymous reviewer for a critical reading of the manuscript and several useful comments and suggestions, which greatly improved the scientific contents of the paper. The research work at Physical Research Laboratory is funded by the Department of Space, Gov-

ernment of India. This work is based on data obtained as part of the UKIRT Infrared Deep Sky Survey. This publication made use of data products from the Two Micron All Sky Survey (a joint project of the University of Massachusetts and the Infrared Processing and Analysis Center / California Institute of Technology, funded by NASA and NSF), archival data obtained with the *Spitzer* Space Telescope (operated by the Jet Propulsion Laboratory, California Institute of Technology under a contract with NASA). NANTEN2 is an international collaboration of 11 universities: Nagoya University, Osaka Prefecture University, University of Bonn, University of Cologne, Seoul National University, University of Chile, University of New South Wales, Macquarie University, University of Sydney, University of Adelaide, and University of ETH Zurich.

## REFERENCES

- Anathpindika, S. V. 2010, MNRAS, 405, 1431
- Balfour, S. K., Whitworth, A. P., & Hubber, D. A. 2017, MNRAS, 465, 3483
- Baug, T., Dewangan, L. K., Ojha, D. K., & Ninan, J. P. 2016, ApJ, 833, 85
- Benjamin, R. A., Churchwell, E., Babler, B. L., et al. 2003, PASP, 115, 953
- Bertoldi, F. 1989, ApJ, 346, 735
- Bisbas, T. G., Wünsch, R., Whitworth, A. P., & Hubber, D. A. 2009, A&A, 497, 649
- Bisbas, T. G., Haworth, T. J., Williams, R. J. R., et al. 2015, MNRAS, 453, 1324
- Bisbas, T. G., Tanaka, K. E. I., Tan, J. C., Wu, B., & Nakamura, F. 2017, ApJ, 850, 23
- Bohlin, R. C., Savage, B. D., & Drake, J. F. 1978, ApJ, 224, 1323
- Bressert, E., Bastian, N., Gutermuth, R., et al. 2010, MNRAS, 409, 54
- Casertano, S., & Hut P. 1985, ApJ, 298, 80
- Churchwell, E., Povich, M. S., Allen, D., et al. 2006, ApJ, 649, 759
- Churchwell, E., Watson, D. F., Povich, M. S., et al. 2007, ApJ, 670, 428
- Condon, J. J., Cotton, W. D., Greisen, E. W., et al. 1998, AJ, 115, 1693
- Dale, J. E., Clark, P. C., & Bonnell, I. A. 2007, MNRAS, 377, 535
- Deharveng, L., Zavagno, A., & Caplan, J. 2005, A&A, 433, 565
- Deharveng, L., Schuller, F., Anderson, L. D., et al. 2010, A&A, 523, 6
- Dewangan, L. K., Ojha, D. K., Anandarao, B. G., Ghosh, S. K., & Chakraborti, S. 2012, ApJ, 756, 151
- Dewangan, L. K., Ojha, D. K., Grave, J. M. C., & Mallick, K. K. 2015a, MNRAS, 446, 2640
- Dewangan, L. K., Luna, A., Ojha, D. K., et al. 2015b, ApJ, 811, 79
- Dewangan, L. K., Ojha, D. K., Luna, A., et al. 2016a, ApJ, 819, 66
- Dewangan, L. K., Ojha, D. K., Zinchenko, I., et al. 2016b, ApJ, 833, 246
- Dewangan, L. K. 2017, ApJ, 837, 44
- Dewangan, L. K., & Ojha, D. K. 2017, ApJ, 849, 65
- Dewangan, L. K., Ojha, D. K., Zinchenko, I., Janardhan, P., & Luna, A. 2017a, ApJ, 834, 22
- Dewangan, L. K., Ojha, D. K., & Zinchenko, I. 2017b, ApJ, 851, 140
- Dewangan, L. K., Ojha, D. K., Zinchenko, I., & Baug, T. 2018a, ApJ, 861, 19
- Dewangan, L. K., Dhanya, J. S., Ojha, D. K., & Zinchenko, I. 2018b, ApJ, 866, 20
- Dobashi, K., Matsumoto, T., Shimoikura, T., et al. 2014, ApJ, 797, 58
- Dyson, J. E., & Williams, D. A. 1980, Physics of the interstellar medium, New York, Halsted Press, 204 p
- Elmegreen, B. G., & Lada, C. J. 1977, ApJ, 214, 725
- Elmegreen, B. G. 1998, in ASP Conf. Ser. 148, Origins, ed. C. E. Woodward, J. M. Shull, & H. A. Thronson, Jr. (San Francisco, CA: ASP), 150
- Enokiya, R., Sano, H., Hayashi, K., et al. 2018, PASJ, 70, S49
- Evans, N. J., II, Dunham, M. M., Jørgensen, J. K., et al. 2009, ApJS, 181, 321
- Fujita, S., Torii, K., Kuno, N., et al. 2017, under review in PASJ, arXiv:1711.01695
- Fujita, S., Torii, K., Tachihara, K., et al. 2018, ApJ, in press, arXiv:1808.00709
- Fukui, Y., Ohama, A., Hanaoka, N., et al. 2014, ApJ, 780, 36
- Fukui, Y., Harada, R., Tokuda, K., et al. 2015, ApJL, 807, L4
- Fukui, Y., Torii, K., Ohama, A., et al. 2016, ApJ, 820, 26
- Fukui, Y., Tsuge, K., Sano, H., et al. 2017, PASJ, 69, L5
- Fukui, Y., Torii, K., Hattori, Y., et al. 2018a, ApJ, 859, 166
- Fukui, Y., Kohno, M., Yokoyama, K., et al. 2018b, PASJ, 70, S41
- Fukui, Y., Kohno, M., Yokoyama, K., et al. 2018c, PASJ, 70, S44
- Fukui, Y., Ohama, A., Kohno, M., et al. 2018d, PASJ, 70, S46
- Furukawa, N., Dawson, J. R., Ohama, A., et al. 2009, ApJL, 696, L115
- Gong, Y., Fang, M., Mao, R., et al. 2017, ApJL, 835, L14
- Gutermuth, R. A., Megeath, S. T., Myers, P. C., et al. 2009, ApJS, 184, 18
- Habe, A., & Ohta, K. 1992, PASJ, 44, 203
- Haid, S., Walch, S., Seifried, D., Wünsch, R., Dinnbier, F., & Naab, T., 2019, MNRAS, 482, 4062
- Hasegawa, T., Sato, F., Whiteoak, J. B., & Miyawaki, R. 1994, ApJL, 429, L77
- Haworth, T. J., Tasker, E. J., Fukui, Y., et al. 2015a, MNRAS, 450, 10
- Haworth, T. J., Shima, K., Tasker, E. J., et al. 2015b, MNRAS, 454, 1634
- Hayashi, K., Sano, H., Enokiya, R., et al. 2018, PASJ, 70, S48
- Henshaw, J. D., Caselli, P., Fontani, F., Jiménez-Serra, I., Tan, J. C., & Hernandez, A. K. 2013, MNRAS, 428, 3425
- Indebetouw, R., Mathis, J. S., Babler, B. L., et al. 2005, ApJ, 619, 931
- Inoue, T., & Fukui, Y. 2013, ApJL, 774, 31
- Kim, K. T., & Koo, B. C. 2001, ApJ, 549, 979
- Kim, K. T., & Koo, B. C. 2003, ApJ, 596, 362
- Kim, Jeong-Gyu, Kim, Woong-Tae, & Ostriker, E. C. 2018, ApJ, 859, 68
- Kohno, M., Torii, K., Tachihara, K., et al. 2018a, PASJ, 70, S50
- Kohno, M., Tachihara, K., Fujita, S., et al. 2018b, PASJ, in press, arXiv:1809.00118
- Kwan, J. 1997, ApJ, 489, 284
- Lada, C. J., & Lada, E. A. 2003, ARA&A, 41, 57
- Lawrence, A., Warren, S. J., Almaini, O., et al. 2007, MNRAS, 379, 1599
- Lefloch, B., & Lazareff, B. 1994, A&A, 289, 559
- Li, C., Wang, H., Zhang, M., et al. 2018, ApJS, 238, 10
- Liu, X.-L., Wang, J.-J., Xu, J.-L., & Zhang, C.-P. 2017, Research in Astronomy and Astrophysics, 17, 35
- Loren, R. B. 1976, ApJ, 209, 466
- Mallick, K. K., Ojha, D. K., Tamura, M., et al. 2015, MNRAS, 447, 2307
- Matsakis, D. N., Evans, N. J., II, Sato, T., & Zuckerman, B. 1976, AJ, 81, 172
- McKee, C. F., & Ostriker, E. C. 2007, ARA&A, 45, 565
- Miyawaki, R., Hayashi, M., & Hasegawa, T. 1986, ApJ, 305, 353
- Miyawaki, R., Hayashi, M., & Hasegawa, T. 2009, PASJ, 61, 39
- Molinari, S., Swinyard, B., Bally, J., et al., 2010, A&A, 518, L100
- Motte, F., Bontemps, S., & Louvet, F. 2018, ARA&A, in press (arXiv:1706.00118)
- Nakamura, F., Miura, T., Kitamura, Y., et al. 2012, ApJ, 746, 25
- Nakamura, F., Sugitani, K., Tanaka, T., et al. 2014, ApJL, 791, L23
- Nishimura, A., Costes, J., Inaba, T., et al. 2017, under review in PASJ, arXiv:1706.06002
- Nishimura, A., Minamidani, T., Umamoto, T., et al. 2018, PASJ, 70, S42
- Ohama, A., Dawson, J. R., Furukawa, N., et al. 2010, ApJ, 709, 975
- Ohama, A., Tsutsumi, D., Sano, H., et al. 2017, under review in PASJ, arXiv:1706.05652
- Ohama, A., Kohno, M., Hasegawa, K., et al. 2018a, PASJ, 70, S45
- Ohama, A., Kono, M., Fujita, S., et al. 2018b, PASJ, 70, S47



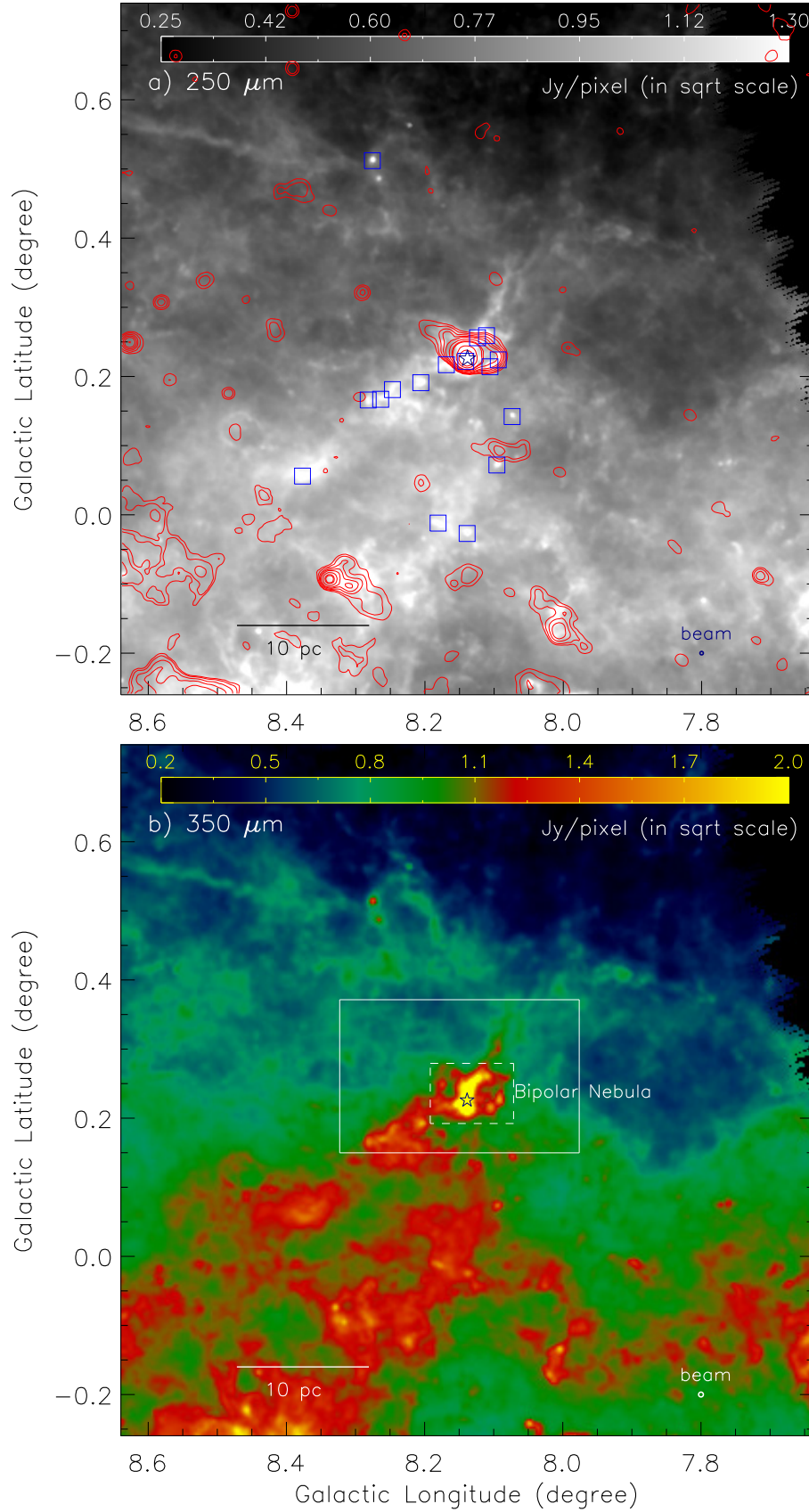


**Figure 1.** a) Overlay of the NVSS 1.4 GHz radio continuum emission contours (in red) and sixteen ATLASGAL 870  $\mu\text{m}$  dust continuum clumps (blue squares; from Urquhart et al. 2018) on the *Herschel* image at 250  $\mu\text{m}$  (size  $\sim 1^\circ \times 1^\circ$ ; centered at  $l = 8^\circ.14$ ;  $b = 0^\circ.24$ ). The NVSS contours are shown with the levels of  $0.45 \text{ mJy/beam} \times (8, 15, 30, 50, 80, 160, 290, 350, 900, 1800)$ . All the ATLASGAL clumps are depicted in a velocity range of  $[15, 21] \text{ km s}^{-1}$ , and are located at a distance of 3.0 kpc (see Urquhart et al. 2018). b) A false color *Herschel* image at 350  $\mu\text{m}$ . A solid box (in white) highlights the area studied in Paper II. A dashed box (in white) indicates the previously known BPN (see also Figure 2b). In each panel, a star symbol (in navy) indicates the position of the 6.7 GHz maser. The scale bar corresponding to 10 pc (at a distance of 3.0 kpc) is displayed in both the panels. In each panel, a small circle represents the beam size of the *Herschel* image.



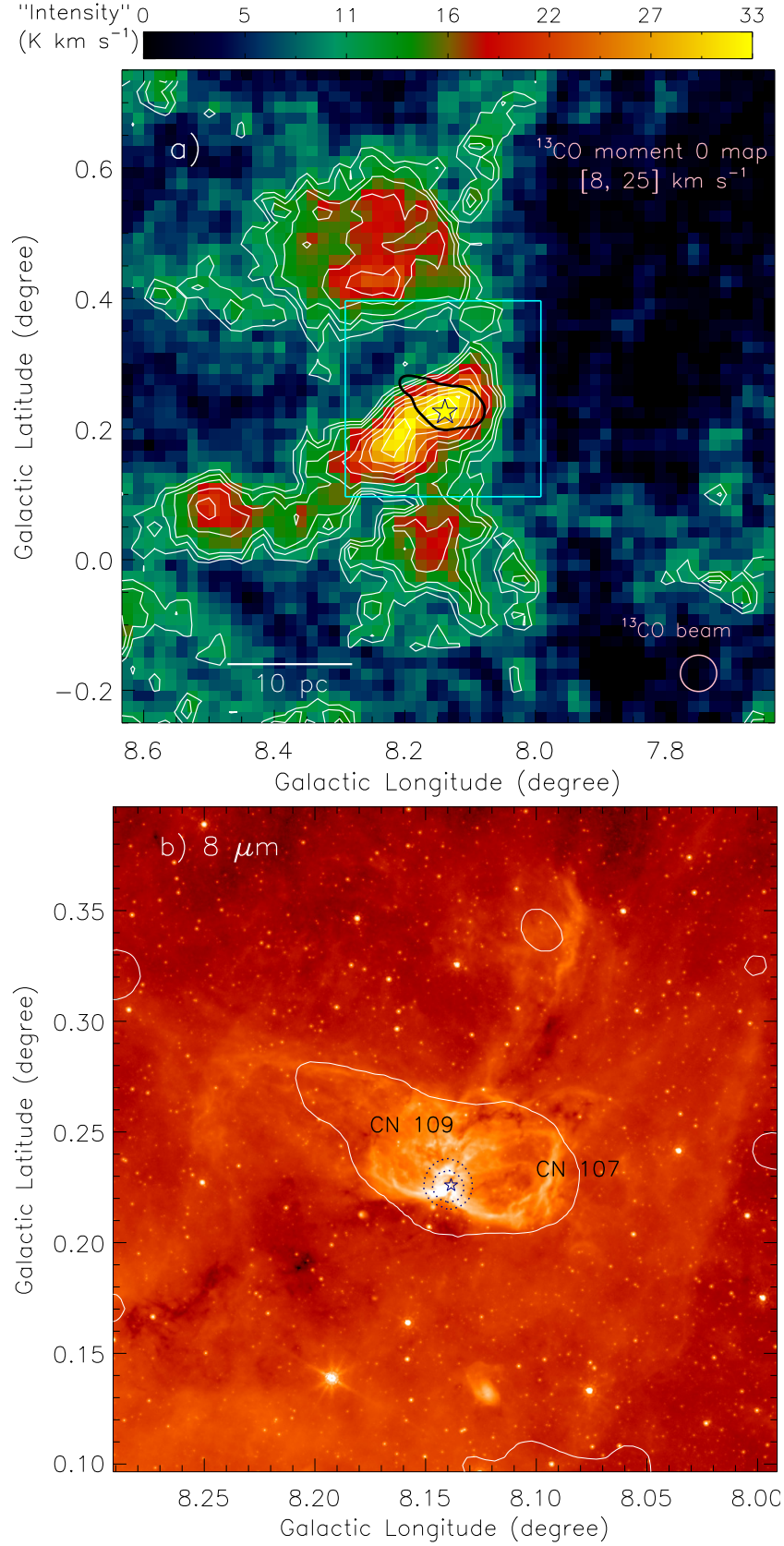


**Figure 2.** a) The NANTEN2  $^{13}\text{CO}(J=1-0)$  intensity map (moment-0) integrated over the velocity range of  $[8, 25] \text{ km s}^{-1}$ . The map is also overlaid with the  $^{13}\text{CO}$  intensity contours (in white) at  $34.5 \text{ K km s}^{-1} \times (0.3, 0.35, 0.4, 0.5, 0.6, 0.7, 0.8, 0.9, \text{ and } 0.98)$ , where  $1\sigma \sim 2.3 \text{ K km s}^{-1}$ . The bar at the top indicates the color-coded intensity in  $\text{K km s}^{-1}$ . The NVSS 1.4 GHz radio continuum emission contour (in black) is shown with a level of  $8\sigma$ , where  $1\sigma = 0.45 \text{ mJy/beam}$ . A small circle (in pink) shows the beam size of the  $^{13}\text{CO}$  line data. b) The panel displays a false color *Spitzer*  $8 \mu\text{m}$  image of an area highlighted by a broken box in Figure 2a. The map is also superimposed with the NVSS 1.4 GHz radio emission contours (see white solid and black dotted contours). The white solid contour is the same as in Figure 2a, while the black dotted contours are plotted with the levels of 0.81 and 1.44  $\text{Jy/beam}$ . Two MIR bubbles CN 107 and CN 109 (from Churchwell et al. 2007) are also labeled in the image. In each panel, a star symbol (in navy) indicates the position of the 6.7 GHz maser.

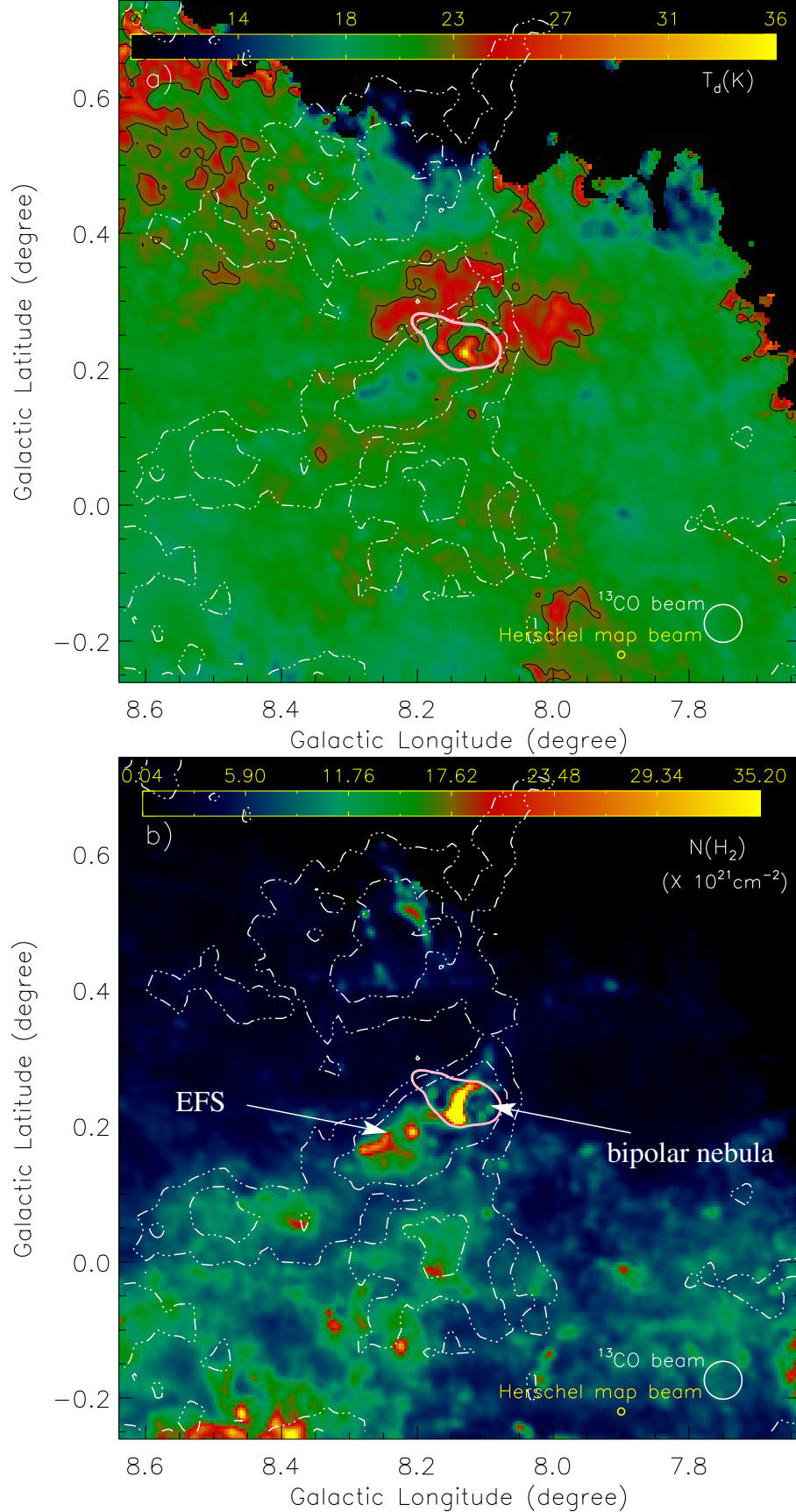


**Figure 3.** a) The panel displays the *Herschel* temperature map of the G8.14+0.23 H II region. The temperature of 23 K contour (in black) is also overlaid on the *Herschel* map. b) The panel displays the *Herschel* column density ( $N(\text{H}_2)$ ) map of the G8.14+0.23 H II region. In each panel, the integrated  $^{13}\text{CO}$  emission contours at [8, 25]  $\text{km s}^{-1}$  (see white dotted-dashed contours) are overplotted with the levels of 10.35 ( $4.5\sigma$ ) and 16.66 ( $7.2\sigma$ )  $\text{K km s}^{-1}$  (see also Figure 2a). The NVSS 1.4 GHz radio continuum emission contour (in pink) is shown with a level of 0.45  $\text{mJy/beam} \times 8$  in both the panels. In each panel, a big circle (in white) and a small circle (in yellow) show the beam sizes of the  $^{13}\text{CO}$  line data and the *Herschel* column density map, respectively.

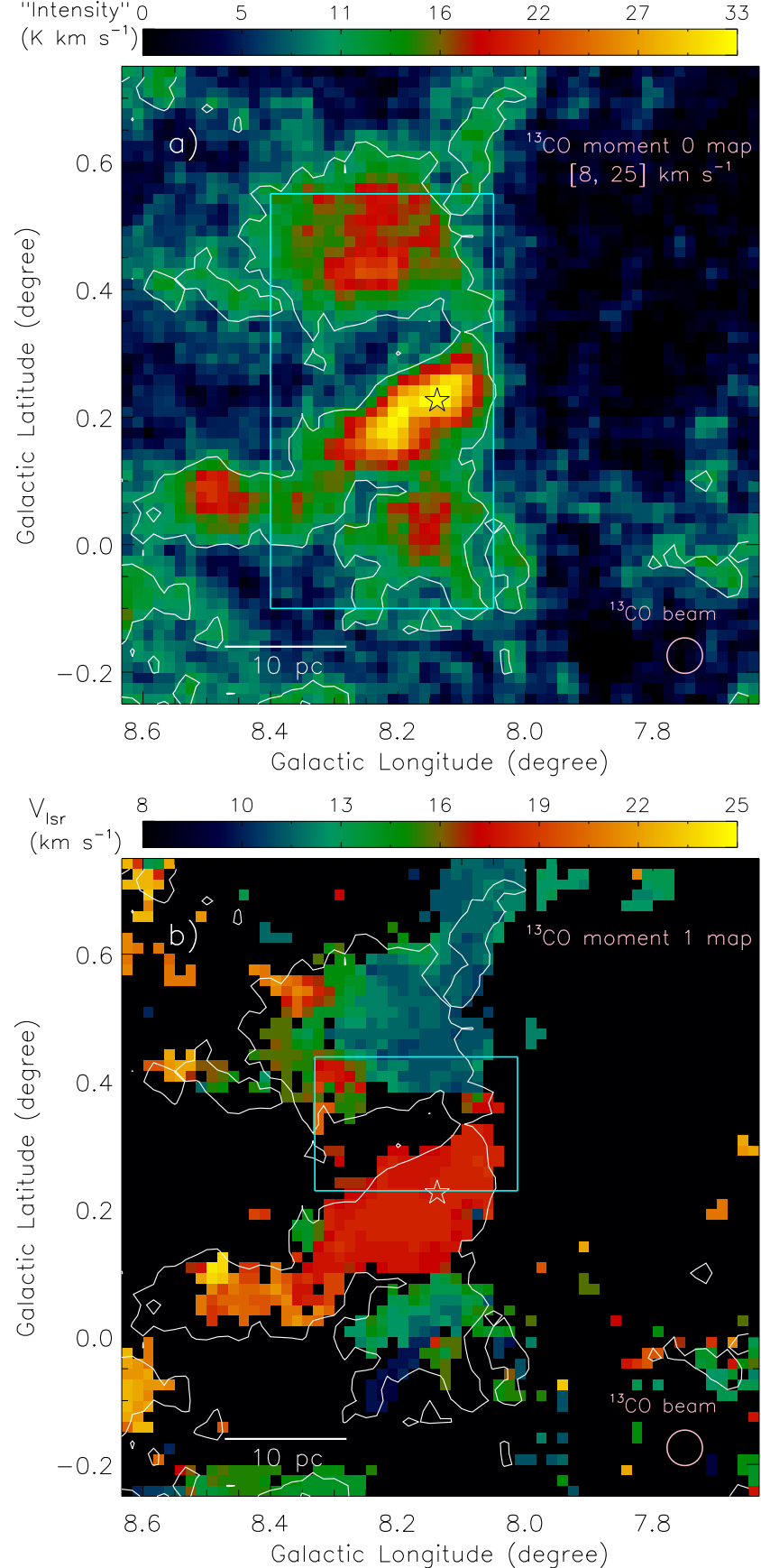


**Figure 4.** a)  $^{13}\text{CO}$  intensity map (moment-0) integrated over the velocity range of [8, 25]  $\text{km s}^{-1}$  (see also Figure 2a). The area highlighted by a solid box (in cyan) is used for extracting the position-velocity maps (see Figures 6a and 6b). b) Intensity-weighted mean velocity (moment-1) map of  $^{13}\text{CO}$ . The  $^{13}\text{CO}$  emission integrated over the velocity range of [8, 25]  $\text{km s}^{-1}$  and clipped at the  $4.8\sigma$  rms level of  $\sim 0.44$  K per channel. The area highlighted by a solid box (in cyan) is used for extracting the  $^{13}\text{CO}$  profile (see Figure 6d). In both the panels, the  $^{13}\text{CO}$  emission contour at [8, 25]  $\text{km s}^{-1}$  is also overlaid with a level of 10.35  $\text{K km s}^{-1}$  ( $4.5\sigma$ ; see also Figure 2a). In each panel, a star symbol indicates the position of the 6.7 GHz maser, and a big circle (in pink) shows the beam size of the  $^{13}\text{CO}$  line data.

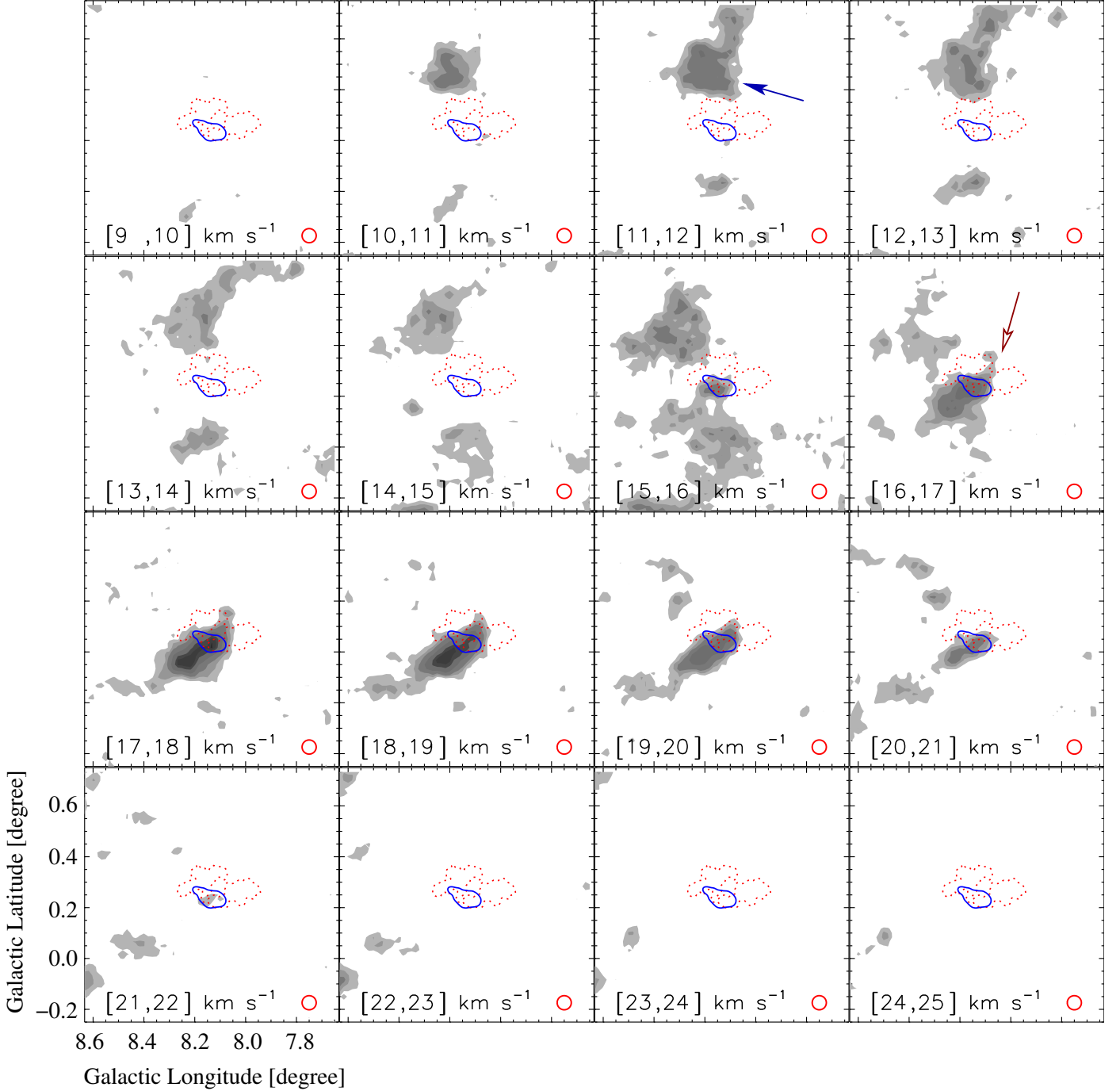


**Figure 5.**  $^{13}\text{CO}(J=1-0)$  velocity channel contour maps. The molecular emission is integrated over a velocity interval, which is labeled in each panel (in  $\text{km s}^{-1}$ ). In all the panels, the contours are shown with the levels of 2.0, 3.0, 4.0, 6.0, 8.0, 9.0, and  $10 \text{ K km s}^{-1}$ . In all the panels, the NVSS 1.4 GHz radio continuum emission contour (in blue) toward the G8.14+0.23 H II region is shown with a level of  $0.45 \text{ mJy/beam} \times 8$ . In each panel, the *Herschel* temperature contour at 23 K is also shown (see dotted red contour and also Figure 3a). Arrows highlight molecular gas in two cloud components. In each panel, a thick circle (in red) shows the beam size of the  $^{13}\text{CO}$  line data.

Okumura, S.-I., Miyawaki, R., Sorai, K., Yamashita, T., & Hasegawa, T. 2001, PASJ, 53, 793  
Panagia, N. 1973, AJ, 78, 929  
Saigo, K., Onishi, T., Nayak, O., et al. 2017, ApJ, 835, 108  
Sano, H., Torii, K., Saeki, S., et al. 2017, under review in PASJ, arXiv:1708.08149  
Sano, H., Enokiya, R., Hayashi, K., et al. 2018, PASJ, 70, S43  
Sato, F., Hasegawa, T., Whiteoak, J. B., & Miyawaki, R. 2000, ApJ, 535, 857  
Schuller, F., Menten, K. M., Contreras, Y., et al. 2009, A&A, 504, 415

Shimoikura, T., & Dobashi, K. 2011, ApJ, 731, 23  
Shimoikura, T., Dobashi, K., Saito, H., et al. 2013, ApJ, 768, 72  
Skrutskie, M. F., Cutri, R. M., Stiening, R., et al. 2006, AJ, 131, 1163  
Szymczak, M., Wolak, P., Bartkiewicz, A., & Borkowski, K. M. 2012, AN, 333, 634  
Tachihara, K., Gratier, P., Sano, H., et al. 2018, PASJ, 70, S52  
Takahira, K., Tasker, E. J., & Habe, A. 2014, ApJ, 792, 63  
Takahira, K., Shima, K., Habe, A., & Tasker, E. J. 2018, PASJ, 70, S58  
Takeuchi, T., Yamamoto, H., Torii, K., et al. 2010, PASJ, 62, 557

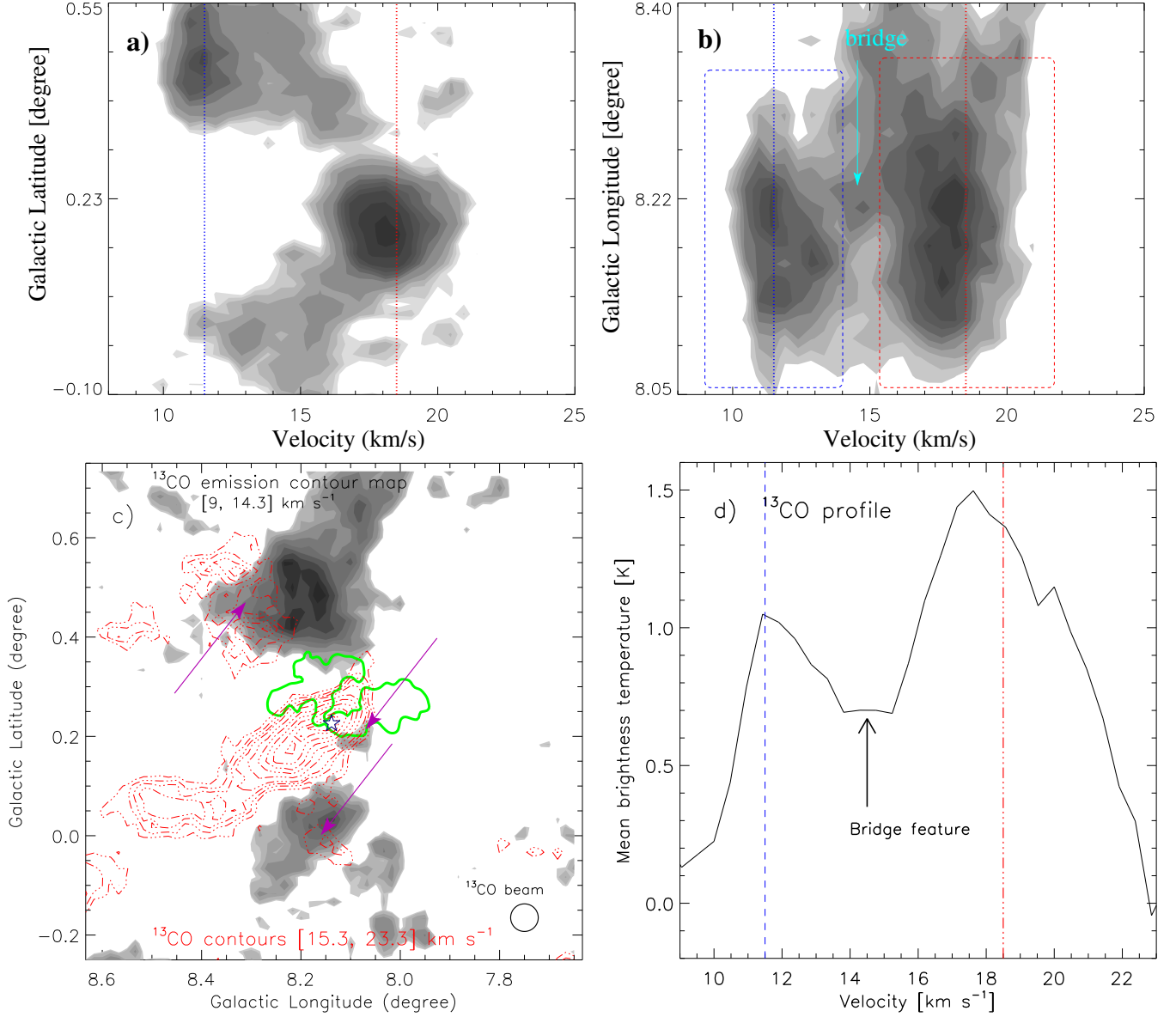


**Figure 6.** a) Latitude-velocity map of  $^{13}\text{CO}$  (see a solid box in Figure 4a). The  $^{13}\text{CO}$  emission is integrated over the longitude range from  $8^{\circ}.05$  to  $8^{\circ}.40$ . The contour levels are 18, 20, 22, 25, 30, 40, 45, 50, 55, 60, 70, 80, 90, and 100 deg K, where  $1\sigma \sim 2$  deg K. b) Longitude-velocity map of  $^{13}\text{CO}$  (see a solid box in Figure 4a). The  $^{13}\text{CO}$  emission is integrated over the latitude range from  $-0^{\circ}.10$  to  $0^{\circ}.55$ . The contour levels are 30, 35, 40, 45, 50, 55, 60, 65, 70, and 72 deg K, where  $1\sigma \sim 2.7$  deg K. Two broken boxes indicate two cloud components. c) The  $^{13}\text{CO}$  emissions integrated over two different velocity ranges at  $[9, 14.3]$  and  $[15.3, 23.3]$  km s $^{-1}$  are presented, and the velocity ranges are also given in the figure. The contour levels of the background  $^{13}\text{CO}$  emission map at  $[9, 14.3]$  km s $^{-1}$  are 3.87, 4.15, 4.84, 5.53, 6.91, 8.30, 9.68, 11.06, 12.44, and 13.14 K km s $^{-1}$ , where  $1\sigma \sim 1.2$  K km s $^{-1}$ . The broken contours tracing the cloud at  $[15.3, 23.3]$  km s $^{-1}$  (in red) are shown with the levels of 7.87, 9.45, 11.02, 12.60, 15.75, 18.89, 22.04, 25.19, 28.34, and 29.92 K km s $^{-1}$ , where  $1\sigma \sim 1.3$  K km s $^{-1}$ . The temperature of 23 K contour (in green) is also shown in the figure. A star symbol indicates the position of the 6.7 GHz maser, and a big circle (in black) shows the beam size of the  $^{13}\text{CO}$  line data. d) The  $^{13}\text{CO}$  profile in the direction of an area highlighted by a solid box in Figure 4b. The profile is produced by averaging the area shown in Figure 4b. An arrow indicates an almost flattened spectrum between two velocity peaks. In panels “a”, “b”, and “d”, two velocities (i.e., 11.5 and 18.5 km s $^{-1}$ ) are highlighted by two dotted lines.

Tan, J. C., Beltrán, M. T., Caselli, P., et al. 2014, in *Protostars and Planets VI*, ed. H. Beuther et al. (Tucson, AZ: Univ. Arizona Press), 149  
 Torii, K., Enokiya, R., Sano, H., et al. 2011, *ApJ*, 738, 46  
 Torii, K., Hasegawa, K., Hattori, Y., et al. 2015, *ApJ*, 806, 7  
 Torii, K., Hattori, Y., Hasegawa, K., et al. 2017a, *ApJ*, 835, 142  
 Torii, K., Hattori, Y., Hasegawa, K., et al. 2017b, *ApJ*, 840, 111  
 Torii, K., Fujita, S., Matsuo, M., et al. 2018a, *PASJ*, 70, S51  
 Torii, K., Hattori, Y., Matsuo, M., et al. 2018b, *PASJ*, in press, arXiv:1706.07164  
 Tsuboi, M., Miyazaki, A., & Uehara, K. 2015, *PASJ*, 67, 109

Tsuge, K., Sano, H., Tachihara, K., et al. 2018, *ApJ*, in press, arXiv:1803.00713  
 Tsutsumi, D., Ohama, A., Okawa, K., et al. 2017, under review in *PASJ*, arXiv:1706.05664  
 Urquhart, J. S., Moore, T. J. T., Schuller, F., et al. 2013, *MNRAS*, 431, 1752  
 Urquhart, J. S., König, C., Giannetti, A., et al. 2018, *MNRAS*, 437, 1059  
 Walch, S., Whitworth, A. P., Bisbas, T. G., Hubber, D. A., & Wünsch, R. 2015, *MNRAS*, 452, 2794  
 Walsh, A. J., Burton, M. G., Hyland, A. R., & Robinson, G. 1998, *MNRAS*, 301, 640



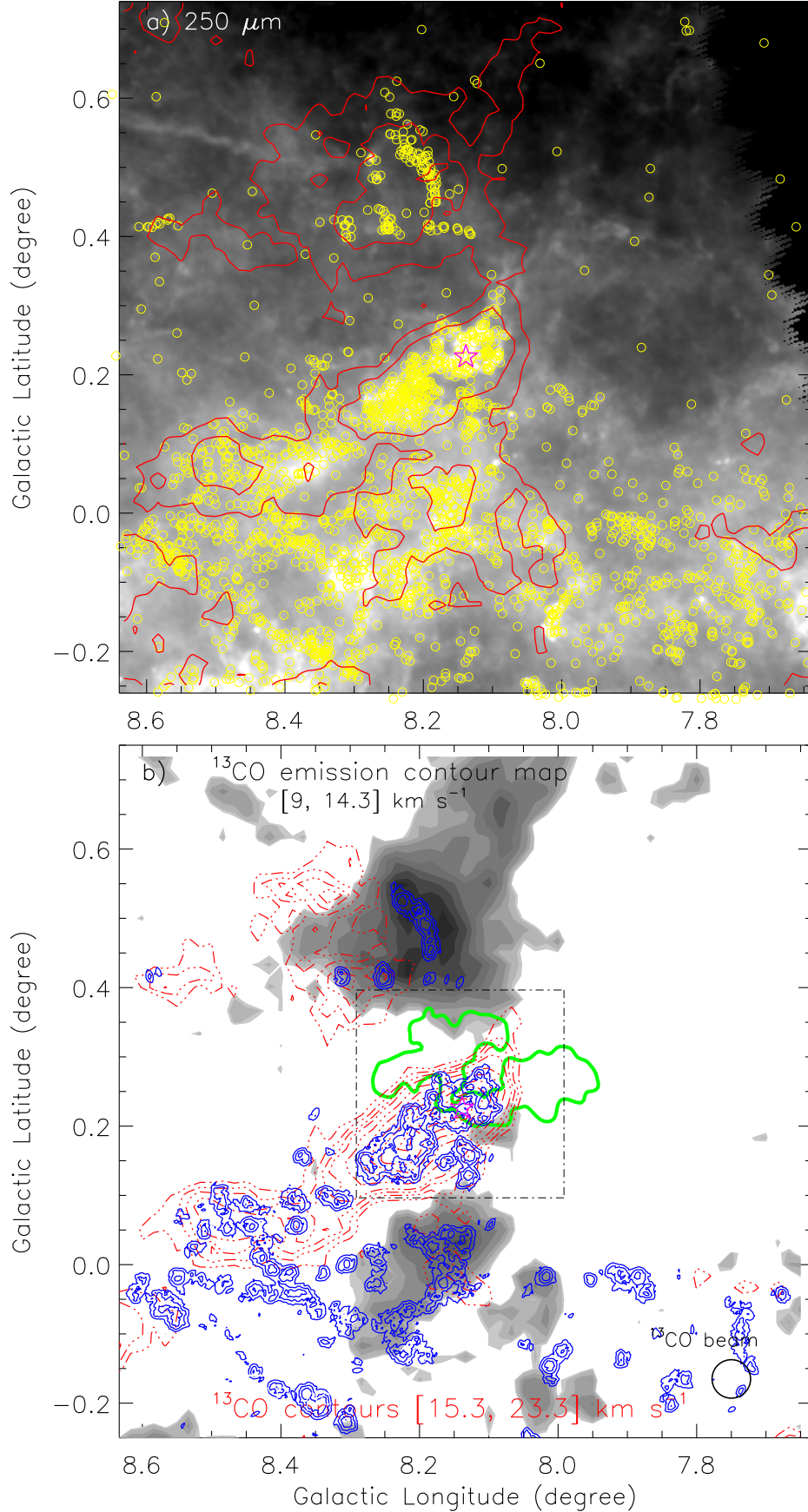


**Figure 7.** a) Overlay of sources with  $H-K > 2.2$  mag (see yellow circles) on the *Herschel* 250  $\mu\text{m}$  image. The  $^{13}\text{CO}$  emission contours at  $[8, 25] \text{ km s}^{-1}$  are also overlaid on the *Herschel* image, and are shown with the levels of  $10.35 \text{ K km s}^{-1}$  ( $4.5\sigma$ ) and  $16.66 \text{ K km s}^{-1}$  ( $7.2\sigma$ ). b) Overlay of surface density contours of sources with  $H-K > 2.2$  mag (see yellow circles in Figure 7a) on the integrated intensity maps of  $^{13}\text{CO}$  (at  $[9, 14.3]$  and  $[15.3, 23.3] \text{ km s}^{-1}$ ). The molecular maps are the same as in Figure 6c. The surface density contours (in blue) are plotted with the levels of 3, 5, and 10  $\text{YSOs pc}^{-2}$ . The *Herschel* temperature emission at 23 K is shown with a thick curve (in green; see also Figure 3a). In each panel, a star symbol (in magenta) indicates the position of the 6.7 GHz maser.

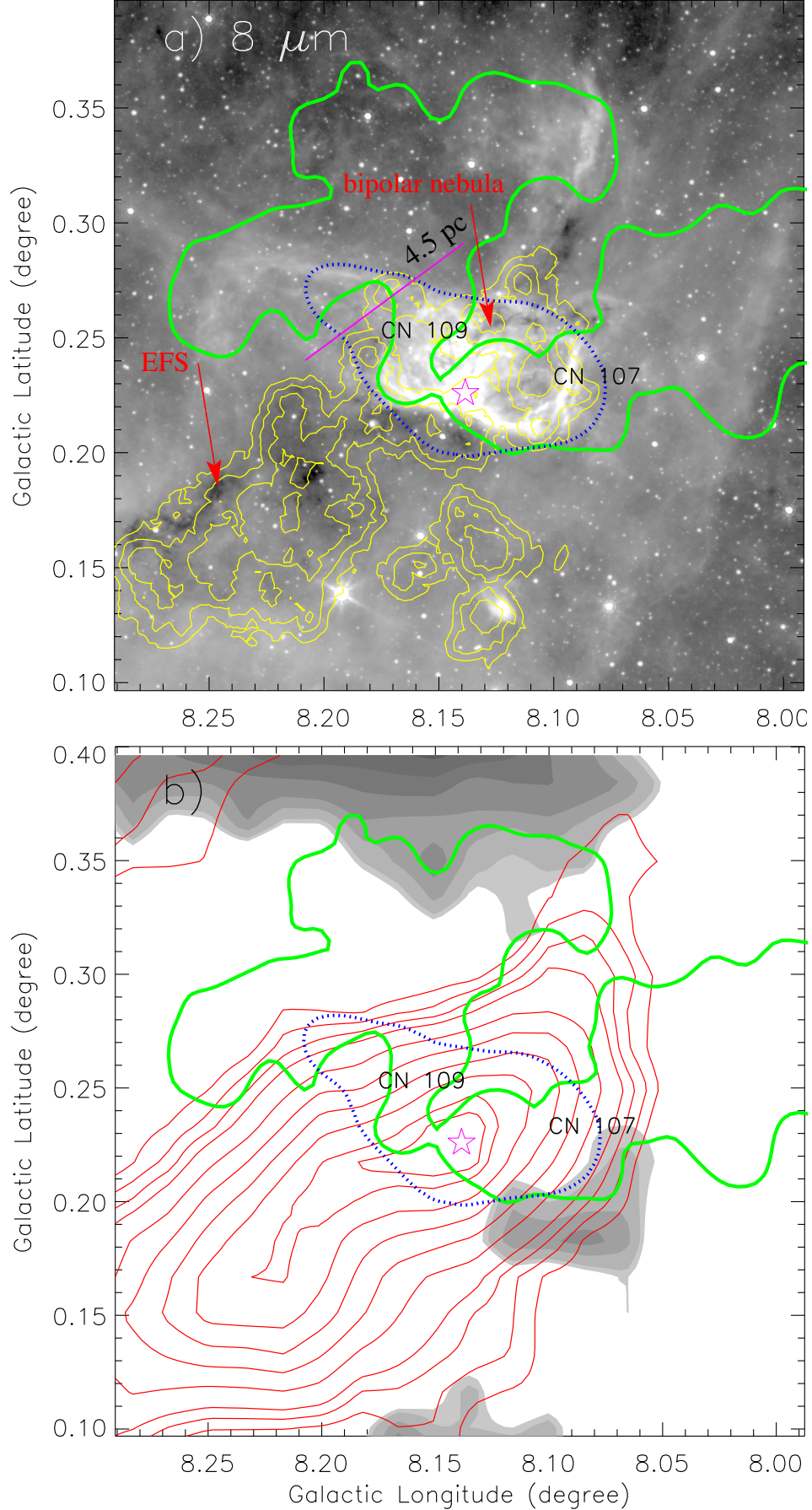


**Figure 8.** A zoomed-in view of the G8.14+0.23 HII region (see a broken box in Figure 7b). a) Overlay of surface density contours of sources (in yellow) on the *Spitzer* 8  $\mu\text{m}$  image (see also Figure 7b). The surface density contours are the same as in Figure 7b. b) Spatial distribution of two clouds at [9, 14.3] and [15.3, 23.3] km s<sup>-1</sup> (see a broken box in Figure 7b). The molecular emission contours are the same as in Figure 7b. In each panel, a star symbol (in magenta) indicates the position of the 6.7 GHz maser. In both the panels, the NVSS 1.4 GHz radio continuum emission contour (in blue) and the *Herschel* temperature contour at 23 K (in green) are also drawn.



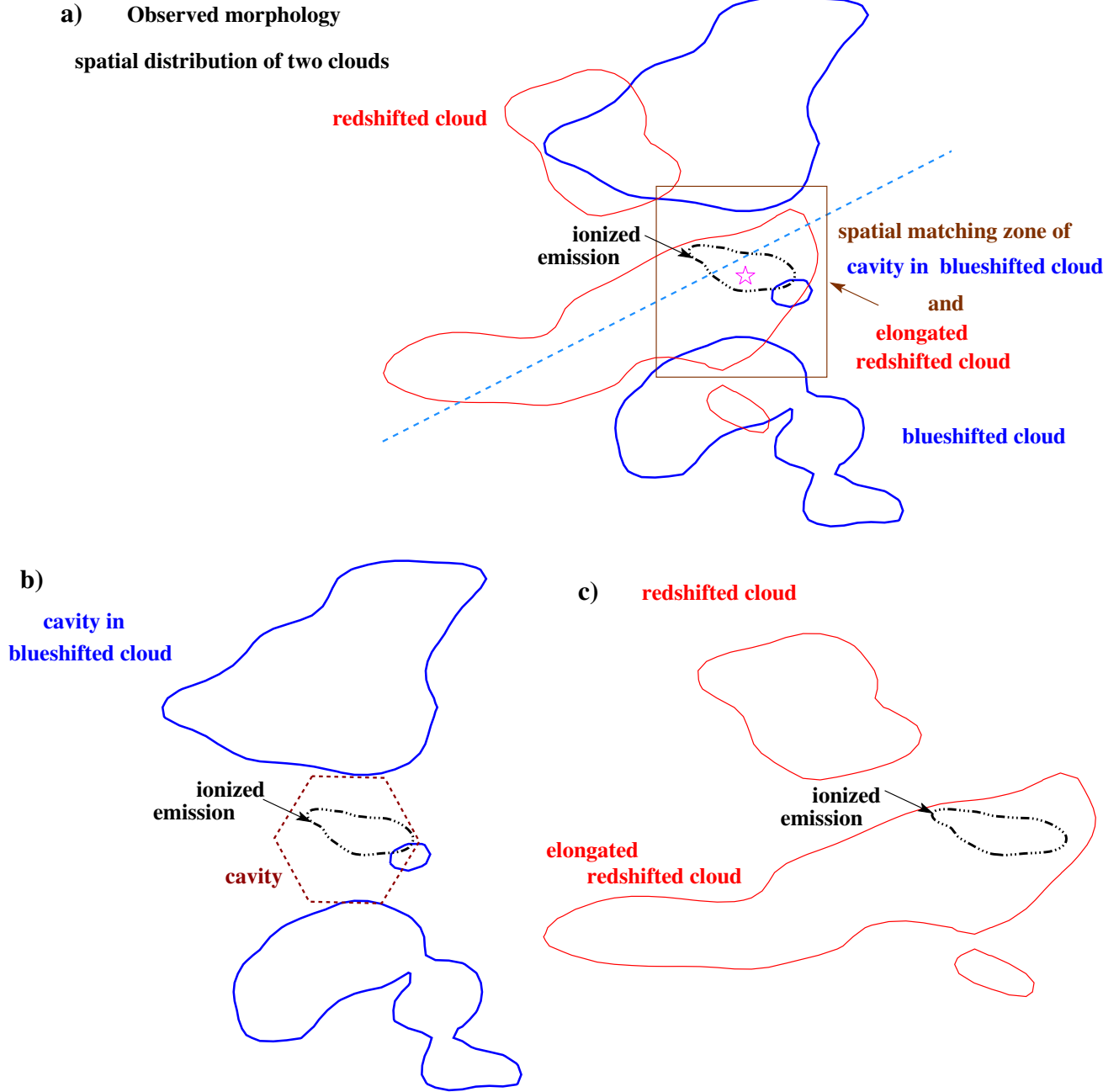


**Figure 9.** a) The panel displays the spatial distribution of redshifted and blueshifted clouds. A dotted-dashed contour (in black) represents the location of the H II region. A star symbol (in magenta) indicates the position of the 6.7 GHz maser. A dashed line represents the Galactic eastern-southern to northern-western direction. b) The panel shows the existence of a cavity (or intensity-depression) in the blueshifted cloud. c) The panel highlights the H II region in the redshifted cloud.

Whitworth, A. P., Bhattal, A. S., Chapman, S. J., Disney, M. J., & Turner, J. A. 1994, MNRAS, 268, 291  
 Whitworth, A., Lomax, O., Balfour, S., et al. 2018, PASJ, 70, S.55  
 Wu, B., Van, L. S., Tan, J. C., & Bruderer, S. 2015, ApJ, 811, 56

Wu, B., Tan, J. C., Nakamura, F., Van, L. S., Christie, D., & Collins, D. 2017a, ApJ, 835, 137  
 Wu, B., Tan, J. C., Christie, D., Nakamura, F., Van, L. S., & Collins, D. 2017b, ApJ, 841, 88  
 Zinnecker, H., & Yorke, H. W. 2007, ARA&A, 45, 481